Oceanologia (2020) 62, 347—363

Available online at www.sciencedirect.com

ScienceDirect

journal homepage: www.journals.elsevier.com/oceanologia

ORIGINAL RESEARCH ARTICLE

Measurements of light transfer through drift ice and landfast ice in the northern Baltic Sea

Elina Kari[a,d,*], **Arttu Jutila**[b,e], **Anna Friedrichs**[c], **Matti Leppäranta**[b], **Susanne Kratzer**[a]

[a] *Department of Ecology, Environment and Plant Sciences, Stockholm University, Stockholm, Sweden*
[b] *Institute for Atmospheric and Earth System Research (INAR), University of Helsinki, Helsinki, Finland*
[c] *Institute for Chemistry and Biology for the Marine Environment, Carl von Ossietzky University of Oldenburg, Oldenburg, Germany*
[d] *Present: Institute for Atmospheric and Earth System Research (INAR), P.O. Box 64, 00014 University of Helsinki, Finland*
[e] *Present: Alfred-Wegener-Institut Helmholtz-Zentrum für Polar- und Meeresforschung, Am Handelshafen 12, 27570 Bremerhaven, Germany.*

Received 29 November 2019; accepted 2 April 2020
Available online 20 May 2020

KEYWORDS
Light transfer;
Sea ice;
Diffuse attenuation coefficient;
Coloured dissolved organic matter;
Scattering

Summary The aim of this study was to investigate the light transfer through sea ice with a focus on bio-optical substances both in fast ice and in the drift ice zones in the northern Baltic Sea. The measurements included snow and ice structure, spectral irradiance and photosynthetically active radiation below the sea ice. We also measured the concentrations of the three main bio-optical substances which are chlorophyll-*a*, suspended particulate matter, and coloured dissolved organic matter (CDOM). These bio-optical substances were determined for melted ice samples and for the underlying sea water. The present study provides the first spectral light transfer data set for drift ice in the Baltic Sea. We found high CDOM absorption values typical to the Baltic Sea waters also within sea ice. Our results showed that the transmittance through bare ice was lower for the coastal fast ice than for the drift ice sites. Bio-optical substances, in particular CDOM, modified the spectral distribution of light penetrating through the ice cover. Differences in crystal structure and the amount of gas inclusions in the ice caused variation in the light transfer. Snow cover on ice was found to be the dominant factor influencing the light field under ice, confirming previous studies. In conclusion, snow cover dominated

* Corresponding author at: Institute for Atmospheric and Earth System Research (INAR), P.O. Box 64, 00014 University of Helsinki, Finland.
E-mail address: elina.kari@helsinki.fi (E. Kari).
Peer review under the responsibility of the Institute of Oceanology of the Polish Academy of Sciences.

Production and hosting by Elsevier

https://doi.org/10.1016/j.oceano.2020.04.001

the amount of light under the ice, but did not modify its spectral composition. CDOM in the ice absorbs strongly in the short wavelengths. As pure water absorbs most in the long wavelengths, the light transfer through ice was highest in the green (549—585 nm).

1. Introduction

The Baltic Sea is a shallow, brackish sea with an annual sea ice cover lasting between four to seven months (Leppäranta and Myrberg, 2009). In the northernmost basin, the Gulf of Bothnia, river water dominates the water budget, and the salinity of the upper layer is only 2—6 ppt. The river inflow contains high concentrations of coloured dissolved organic matter (CDOM) — a mixture of dissolved, decomposed organic matter and humic substances that absorb light at short wavelengths (e.g. Arst, 2003; Pierson et al., 2008). CDOM absorption is the main factor determining the attenuation of light in the Baltic Sea (Arst, 2003; Pierson et al., 2008) and is also found to be inversely related to salinity (Harvey et al., 2015; Kari et al., 2018; Kowalczuk et al., 2006; Kratzer et al., 2003). Other substances influencing the underwater light field are suspended particulate matter (SPM) and chlorophyll-*a* (Chl-*a*).

The brackish Baltic Sea ice shows similar characteristics to marine sea ice, such as the development of saline brine channels (Kawamura et al., 2001; Palosuo, 1961; Weeks et al., 1990). As saline water freezes, ice grows downwards in elongated, columnar crystals, i.e. congelation ice. Growing ice also locks substances from the underlying (freezing) seawater into saline brine pockets or channels in between ice crystal plates but may also reject them. The resulting brine channel system forms a key habitat for ice-associated organisms (Huttunen and Niemi, 1986; Ikävalko, 1998; Ikävalko et al., 1994). In addition to columnar ice, granular snow-ice forms from flooded seawater on top of the ice surface (Leppäranta, 1983; Palosuo, 1963). Granular frazil ice may also form, but its occurrence and amount is not well known in the Baltic Sea (Leppäranta and Myrberg, 2009). On a larger scale, Baltic Sea ice cover appears either as a stable coastal landfast ice zone, or as a dynamic, broken drift ice field with a large variability in thickness and structure (Leppäranta and Myrberg, 2009, Leppäranta, 2011).

Due to the efficient capturing of dissolved organic matter by growing sea ice (Palosuo, 1961; Weeks and Ackley, 1986; Weeks et al., 1990), one may anticipate that significant amounts of CDOM are captured in Baltic Sea ice. This is supported by the results of Arst et al. (2006) and Leppäranta et al. (2003). For SPM the situation is not quite as clear since the ice captures SPM both from sea water during freezing and from atmospheric deposition. The concentration of SPM in Baltic Sea ice has been observed to vary strongly but is generally in a similar range as found within the water body (Leppäranta et al., 1998). Transfer of photosynthetically active radiation (PAR) through the coastal landfast ice zone in the Gulf of Finland (Baltic Sea) has been examined by Ehn et al. (2004), Leppäranta et al. (2003), Rasmus et al. (2002) and Uusikivi et al. (2011, 2010). PAR is an essential factor influencing biological processes within and below the sea ice. Snow cover and its properties, sea ice thickness and crystal structure as well as gas inclusions and bio-optical substances within the ice determine the light transfer through the ice.

It is the aim of this study to investigate light transfer through sea ice in the Gulf of Bothnia, both in the fast ice and drift ice zone. Measurements of both spectral irradiance (320—950 nm) and irradiance integrated over the PAR range (400—700 nm) are included. Further studied properties were reflectance, transmittance, diffuse attenuation coefficient, ice and snow structure, and the concentrations of bio-optical substances within the ice and its underlying water. The objective is to compare the local scale properties of fast ice and drift ice and to discuss their effects on the light transfer through ice.

2. Methods

2.1. Study sites

The fieldwork was conducted during March 2016, March 2017 and during May 2018. In 2016, r/v *Aranda* was used to perform ice research in the Bothnian Bay, the northernmost basin of the Baltic Sea. The measurements were taken on 4—8 March 2016 at five drift ice floes (D1—D5; Fig. 1). On 1—3 March 2017, another research campaign was performed within the fast ice zone close to Umeå, Sweden, in the Northern Quark connecting the Bothnian Sea with the Bothnian Bay. The measurements were taken at three locations each visited twice, thus resulting in six measurement stations (sites F1—F6; Fig. 1). General information on the prevailing ice conditions was obtained from the daily ice charts provided by the Swedish Meteorological and Hydrological Institute (SMHI) and the Finnish Meteorological Institute (FMI). On 16 May 2018, a research cruise was performed in the central Bothnian Bay onboard the Swedish Coast Guards' vessel KBV 181 to measure the spectral absorption and scattering properties of sea water and bio-optical substances in the surface water right after the ice melting. During each campaign, temperature and salinity profiles of the water column were obtained with CTD-profilers: RBRconcerto (Ottawa, Canada) at drift ice sites, Aanderaa (Bergen, Norway) at fast ice sites, and SAIV A/S (Bergen, Norway) at the open water site.

2.2. Snow and ice properties

Properties of snow were investigated by digging snow pits (Table 1). On site, the ice structure was visually charac-

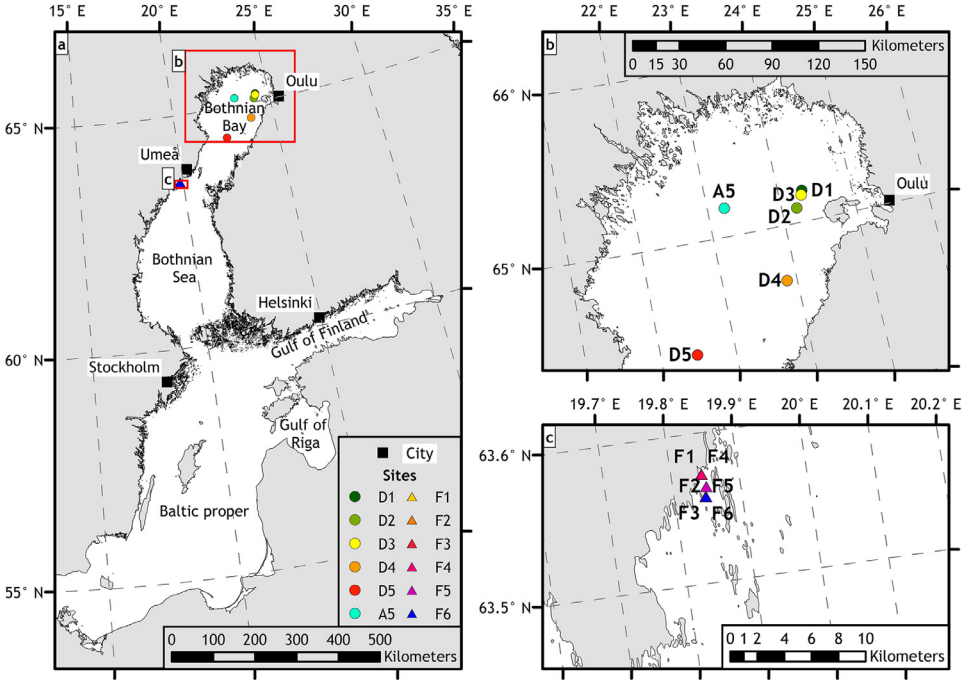

Figure 1 Measurement areas in the Gulf of Bothnia (a). Drift ice sites in the Bothnian Bay (D1–D5) in March 2016 and a site in the open sea (A5) in the central Bothnian Bay in May 2018 (b). Fast ice sites in the northern Bothnian Sea (F1–F6) in March 2017 (c). Background map data: CCM River and Catchment Database © European Commission – JRC, 2007 (Vogt et al., 2007) and SVAR2015 by SMHI.

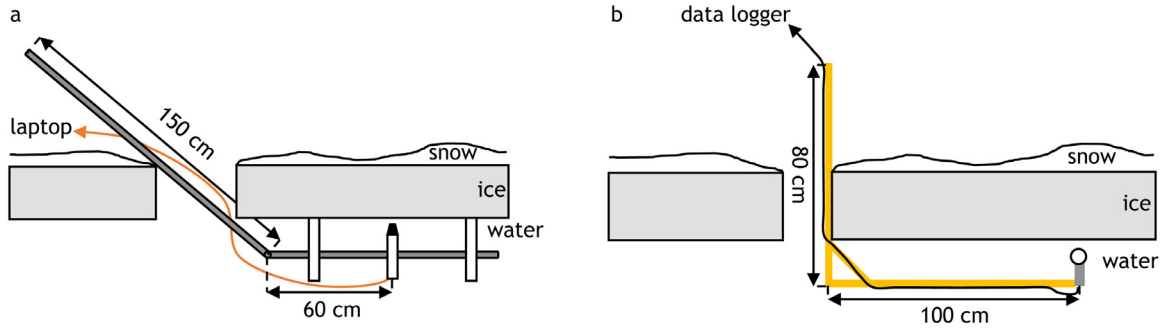

Figure 2 Setups for the irradiance measurements under the ice cover for the drift ice stations (a) and for the landfast ice stations (b). In both cases, the frame kept the sensor vertically levelled and just beneath the bottom of the ice. The frame was directed towards the sun to avoid possible shading.

terised into opaque and transparent ice layers. Ice core samples were taken, placed in plastic tubing, and transported in cold boxes to the freezer (−20°C), where they were stored until further analysis. The fast ice samples were analysed three weeks after sampling and the drift ice samples after 14 months. Ice cores were analysed for their crystal structure. Ice layers were identified from thin sections and classified into granular ice, columnar ice and their transitional form granular/columnar ice (Table 1). The thin sections of ice samples were also photographed. The bulk salinity of the ice cores was measured from the melted ice samples (Table 1). In the fast ice zone, the opaque layer is snow-ice and the transparent layer is columnar congelation ice, but the formation history of the layers in drift ice is not clear.

2.3. Irradiance measurements

Two instrument setups were used for irradiance measurements (Fig. 2; Table 1). At each site, irradiance under the ice was measured both with its natural snow cover and after manually removing the snow. At drift ice sites, the planar spectral irradiance was measured at about 1.5 m above the ice and just beneath the ice (Planar Hyper-spectral radiometer RAMSES ACC-2 VIS, Trios Inc., Germany). At fast ice sites, scalar PAR irradiance was measured at 1 m above the ice and just beneath the ice (Scalar quantum sensor LI-193, LI-COR Biosciences Ltd., UK). The measurements under the ice were first performed with a natural snow surface by lowering the frame through a 40 × 40 cm hole, with minimum disturbances on the snow surface. The instrument was

Table 1 Overview of measuring methods of each parameter used at drift ice sites (D1–D5), at landfast ice sites (F1–F6), and open sea station (A5).

Parameter	Stations	Method
Snowpack structure	D1–D5 FI–F6	Snow pits including snow grain type and size, and layer thickness.
Ice structure	D1–D5 FI–F6	Thin section analysis in a cold room, 'hard hot-plate' technique (Shokr and Sinha, 2015; Weeks and Hibler, 2010).
Ice salinity	D1–D5	Bulk salinity of the melted ice core sample: IntelliCAL™ CDC401 Rugged Conductivity Probe (Hach Lange, Düsseldorf, Germany).
	F1–F6	Bulk salinity of the melted ice core sample: MS-310e Micro-Salinometer (RBR Ltd, Ottawa, Ontario, Canada). Absolute salinity (g kg^{-1}, ppt) was calculated according to the Thermodynamic Equation of Seawater 2010 (TEOS-2010) (McDougall and Barker, 2011).
Spectral irradiance [W m^{-2} nm^{-1}]	D1–D5	Two planar hyperspectral radiometers RAMSES ACC-2 VIS (Trios Inc., Germany), one as a reference instrument. Wavelength window 320–950 nm with spectral resolution of 3.3 nm. Attached to an aluminium frame with polystyrene floats (Fig. 2a). Sensor vertically levelled, close to the bottom of ice, and at about 1 m distance from the drilled hole (Lei et al., 2011).
Quantum irradiance (PAR) [μmol s^{-1} m^{-2}]	F1–F6	Scalar quantum sensor LI-193 and a planar sensor LI-192 as a reference instrument (LI-COR Biosciences Ltd., UK). Integrated quantum irradiance in PAR band (400–700 nm) attached to a wooden setup with a fixed 90° angle (Fig. 2b). Instrument vertically aligned and at 1 meter distance from the drilled hole.
SPM [g m^{-3}]	D1–D5 FI–F6	Measured gravimetrically (Doerffer, 2002; Kratzer et al., 2000; Strickland and Parsons, 1972) by filtering the water sample through a pre-prepared (rinsed with ultra-pure water and combusted) GF/F-filter with 0.7 μm nominal pore size. Filters were dried at 60°C and weighed, to determine the total SPM concentration and combusted at 480°C to determine also the inorganic and organic fractions of the total SPM.
CDOM: g_{440} [m^{-1}]	D1–D5 FI–F6	Filtered through 0.2 μm membrane filter with a mild vacuum of 200 mbar. Filtered samples were stored cooled (max 6°C). CDOM absorption determined with double beam photospectrometer Shimadzu UVPC 2401 (Kyoto, Japan) (Kratzer and Tett, 2009).
Chl-*a* [μg l^{-1}]	D1–D5 FI–F6	Filtered through Whatman GF/F-filters (glass microfiber filters) with a nominal 0.7 μm pore size with a mild vacuum of 200 mbar. Filters were frozen in liquid nitrogen during the drift ice campaign and in −80°C during the fast ice field campaign. Chl-*a* was extracted in 5 ml of 90% acetone, sonicated for 30 seconds and centrifuged to separate the Chl-*a* extract from cell and filter debris. Chl-*a* absorption determined with a double beam spectrophotometer Shimadzu UVPC 2401 (Kyoto, Japan) (Kratzer and Tett, 2009).
Absorption [m^{-1}] Scattering [m^{-1}]	A5	Absorption and scattering were measured *in situ* using a Wetlabs AC9 (USA). Absorption and attenuation readings were corrected for salinity and temperature measured with a SAIV-AS CTD (Norway). Spectral scattering was derived for the nine AC9 wavebands from the difference between spectral beam attenuation and absorption (Kratzer and Moore, 2018).

aligned horizontally by a frame directed towards the sun to avoid possible shading (Fig. 2). Then, the snow was removed from a 3.5 × 3 m area, elongated towards the sun, and then the irradiance was measured below bare ice. In the highly varying ice and snow conditions of the drift ice sites, it was generally challenging to estimate the shading effect caused by ridges. The measurement points were chosen as to keep sufficient distance from surrounding ridges. Such challenges did not occur at the fast ice sites as the ice surface was level within short distances (1–2 m).

A reference instrument was placed on ice five meters away from the sampling site, also facing towards the sun in order to account for possible changes in downwelling irradiance during the period of measurement (at drift ice sites: Ramses ACC-2 VIS, Trios Inc., Germany, and at fast ice sites: a planar sensor LI-192 LI-COR Biosciences Ltd., UK).

The proportional change between subsequent control measurements was used to estimate temporal changes in the irradiance field and to adjust the actual measurements of incident irradiance in further calculations. The measured variations caused by clouds were accounted for in the light transfer estimates.

The studied optical properties were reflectance, transmittance, and the diffuse light attenuation coefficient. The analyses of these properties were limited either to PAR or to 320–900 nm range due to the relevance for ecological and ocean colour applications but also in order to ensure the quality of the spectral irradiance data (Ohde et al., 2007; Simis and Olsson, 2013; Simon and Shanmugam, 2016; Zibordi and Darecki, 2006). At drift ice sites, the surface reflectance, $R(0^+,\lambda)$, was obtained directly from the measurements: $R(0^+,\lambda) = E_u(0^+,\lambda) \,/\, E_d(0^+,\lambda)$, where $E_u(0^+,\lambda)$ is the upwelling and $E_d(0^+,\lambda)$ the downwelling irradiance, just above the surface, and λ is wavelength. The vertical axis is positive in the upward direction (with zero at the ice surface) and the notation $0+$ refers to just above the surface.

At the fast ice sites, scalar quantum PAR irradiance, q_{PAR}, was measured above and below the ice (Table 1). As a scalar instrument measures the radiance evenly from all directions, upwelling irradiance had to be accounted for when estimating the downwelling irradiance. The downwelling irradiance was assumed diffuse above the ice surface during cloud cover and below the ice due to the high scattering in snow and ice (Arst et al., 2006; Leppäranta et al., 2003). Consequently, we have

$$q_{PAR} = q_{d,PAR} + q_{u,PAR} = (1 + R_{PAR}) q_{d,PAR}, \tag{1}$$

where the subscripts d and u refer to downwelling and upwelling irradiance and R_{PAR} is PAR band reflectance. Since no upwelling irradiance measurements were taken, surface reflectance, $R(0^+,\lambda)$, was based on visual evaluation and using literature sources: 0.2 for flooded sea ice, 0.3 for wet ice, 0.5 for wet snow, and 0.85 for new snow (Arst et al., 2006; Leppäranta, 2015; Rasmus et al., 2002). Under ice, the ratio of planar to scalar irradiance, q_p/q_s, was described according to the study by Arst et al. (2006). Backscatter from the water column below was determined in their study as $1 - (q_p/q_s)$. The ratio was assumed to be 0.5 (See Fig. 5a in Arst et al., 2006). Using Equation (1), an estimate of planar downwelling PAR irradiance ($q_{d,PAR}$) can be obtained and this estimate is then used in further calculations of transmittance and light attenuation.

Transmittance of irradiance through the ice cover was defined as the ratio of the downwelling irradiance under the ice, $E_d(-H,\lambda)$, where H is the total ice thickness, to the downwelling irradiance just above the surface, $E_d(0^+,\lambda)$: $T(-H,\lambda) = E_d(-H,\lambda) \,/\, E_d(0^+,\lambda)$. Light attenuation through snow and ice was defined in analogy with the Beer-Lambert absorption law (Perovich, 1996), which describes the exponential decay of light with increasing depth:

$$E_d(-H,\lambda) = \left[1 - R(0^+,\lambda)\right] E_d(0^+,\lambda) \exp\left[-\int_{-H}^{0} K_d(z,\lambda)\,dz\right], \tag{2}$$

where z is depth and K_d is the diffuse attenuation coefficient. Equation (2) has two apparent optical properties: surface reflectance and diffuse attenuation coefficient, which depend on the inherent optical properties of the ice itself and the illumination conditions. For the diffuse attenuation coefficient, a layered profile was assumed with fixed values for snow and ice, $K_{d,snow}$ and $K_{d,ice}$, respectively. Thus,

$$\int_{-H}^{0} K_d(z,\lambda)\,dz = K_{d,tot} H = K_{d,snow} h_s + K_{d,ice} h_i, \tag{3}$$

where h_s and h_i are the thicknesses of snow and ice, respectively. $K_{d,tot}$ was calculated based on measurements through the snow and ice cover and $K_{d,ice}$ referring to the measurements after manually removing the snow cover. Next, diffuse attenuation coefficient for snow cover, $K_{d,snow}$, was determined using a specific inversion technique (Eq. 3) by utilising the measured diffuse attenuation coefficients, $K_{d,tot}$ and $K_{d,ice}$ (Leppäranta et al., 2010). The linear regression models, applying the least squares method, were used to solve $K_{d,snow}$ for the drift ice and fast ice groups separately. The calculations were performed over the PAR range and the fit of regression models were tested with a statistical F-test to find out, whether the results are statistically significant (p-value < 0.05).

In order to examine the primary production, the flux of light quanta, or quantum PAR irradiance q_{PAR}, is needed rather than the radiation power. The quantum irradiance was directly measured at the fast ice sites (Table 1), and at the drift ice sites it was calculated from the spectral irradiance measurements according to:

$$q_{PAR} = \frac{1}{hc_0 N} \int_{PAR} \lambda E(\lambda)\,d\lambda, \tag{4}$$

where h is Planck's constant, c_0 is velocity of light in vacuum, and N is Avogadro's number (e.g. Arst, 2003). For white light, the ratio between quantum irradiance and power irradiance is $q_{PAR}/E_{PAR} = 4.6$ μmol J^{-1}.

2.4. Absorption and scattering properties of surface water

The absorption and scattering properties of surface water (at about 1 m depth) were measured using an AC9 (WetLabs, Philomath, USA) at station A5 in the central Bothnian Bay on 16 May 2018 (Table 1). The AC9 had been calibrated against pure water in the laboratory prior the measurements (Kratzer and Moore, 2018). The raw data was calibrated using the device file and the absorption and scattering values were then corrected for pure water from laboratory calibration measurements and for temperature. The absorption data was corrected for scattering assuming that the absorption is a fixed proportion of the scattering. Spectral scattering was derived for the nine AC9 wavebands from the difference between spectral beam attenuation and absorption (Kratzer and Moore, 2018). Spectral diffuse attenuation was derived from a formula described in Kirk (2011) and in Kratzer and Moore (2018).

2.5. Bio-optical substances

The concentrations of bio-optical substances were measured both from melted ice samples and from the samples of the underlying water. The ice samples were stored in a freezer and later melted at room temperature. The water samples were collected from just beneath the ice. The samples were filtered and then analysed for Chl-*a*, SPM, and

CDOM (Table 1). Chl-*a* concentrations and CDOM absorption were obtained from the absorption spectra measured with a spectrophotometer (Kirk, 2011; Kratzer and Tett, 2009). The absorption coefficient at 440 nm, g_{440}, was used for the CDOM absorption. The method and errors are described in detail in Kratzer and Tett (2009) and Harvey et al. (2015). The concentration of SPM was measured gravimetrically. The methodological errors of determining SPM concentration are discussed in Kari et al. (2016). The Chl-*a* concentration was calculated according to the trichromatic method described in detail in Kratzer and Tett (2009) and in Parsons et al. (1984).

3. Results

3.1. Overall ice conditions

The field campaigns were performed during the ice seasons 2015/16 at the drift ice sites and 2016/17 at the fast ice sites. Both seasons were mild as the maximum sea ice extent of the Baltic Sea was 110 000 km^2 on 22 January 2016 and 88 000 km^2 on 15 February 2017 (Jouni Vainio, FMI Ice service, 2019), well below the 1971—2000 median of 157 000 km^2 (Granskog et al., 2006). In March 2016, ice coverage, was high in the Bothnian Bay (90—100%) with large areas of ridged and rafted ice. In the north, the fast ice was 50—65 cm thick. Further out the ice field was consolidated ice of 40—70 cm thickness (Jouni Vainio, FMI Ice service, 2019). Overall, the ice conditions during sampling were quite dynamic at the drift ice sites. In March 2017, ice cover was stable at the fast ice sites with ice thickness of 15—40 cm. During the first sampling day (1 March) drift ice was compressed against the edge of the fast ice but had opened up by the last sampling day (3 March) (Jouni Vainio, FMI Ice service, 2019).

3.2. Temperature and salinity of the water column

At the drift ice sites D1—D4, the water column was mixed down to the bottom to about 30 m depth. At station D5 the water depth was 90 m with a mixed layer down to a thermocline at 35—50 m depth with a temperature step of 1.5°C. A halocline was found at 50—60 m depth, where the salinity increased from 3.0 ppt to 3.5 ppt. At all drift ice sites, the water temperature in the upper 1 m was near the freezing point (from −0.16°C to −0.15°C) with a salinity of 3.0—3.1 ppt. The fast ice sites F1—F6 were located north of the Öre River mouth with a mean discharge of 411 m^3 s^{-1} during 2006—2016 (SMHI open data service) There were also some small streams near the sampling sites adding to the freshwater runoff. Due to the stable ice cover, the runoff formed an under-ice plume. This 1—2 m thick plume was distinct closest to the shore, but reached the outermost station as well. The salinity of the upper 1 m layer increased with distance from the shore from 1.4 ppt (F1) to 4.4 ppt (F3). This under-ice plume signal was clearly visible also in the upper 1 m layer with temperatures decreasing from 1.7°C (F1) to 0.5°C (F3). When revisiting the stations F1—F3 after two days (stations F4—F6) similar patterns were found within the upper 1 m layer, where the salinity increased from 0.9 ppt (F4) to 5.1 ppt (F6) and the temperature decreased from 2.0°C (F4) to 1.9°C (F6). The salinity at F6 corresponds to the normal salinity of the outer basin water.

3.3. Properties of snow and ice

At the drift ice sites, snow thickness varied from less than 1 cm up to 15 cm with distinct spatial variability (Fig. 3). Even at each individual station, the variation was large. At the northernmost stations D1 and D2, there was a 4 cm thick layer of a large-grained depth hoar at the bottom of the snowpack and due to strong adhesion between the snow and ice surface the snow layer could not be fully removed to create a bare ice surface. At most sites, the snow layer consisted of small rounded grains but with a thin layer of freshly fallen new snow at D2 and a thin slush layer at D5. Ice thickness ranged from 23 to 65 cm at the drift ice sites (Fig. 3). Typical to drift ice, the structure of ice cores varied from a single columnar congelation ice layer to a seven-layer system caused by ice floes having rafted on top of each other (Fig. 4a). The ice cores consisted of 0—79% granular ice (mean 46%) and 21—100% columnar ice (mean 54%) (Fig. 4a). The bulk ice salinity ranged from 0.5 to 0.8 ppt (mean 0.7 ppt), i.e. on average only about 21% of the salinity of the underlying water.

At the fast ice sites, the snow was thicker than at the drift ice sites, varying from 5 cm to 16.5 cm (Fig. 3). Snow was mostly wet and even some slush layers were found. Between the measurement dates, snowfall had brought a 3—5 cm layer of new snow at stations F4—F6. Freezing temperatures during nights had created frozen slush layers and even an ice lens was found in the snowpack at F5. The thickness of fast ice ranged from 24—42 cm, decreasing with distance to the shore (Fig. 3). The ice structure was characterized by an upper granular snow-ice layer and a lower columnar congelation ice layer (Fig. 4b), which is typical for fast ice. The snow-ice contribution ranged from 8—27% of the total ice thickness (with a mean of 17%) (Fig. 4b). The bulk ice salinity ranged from 0.04 to 0.7 ppt (mean 0.4 ppt), on average amounting to 9% of the salinity of the underlying water.

3.4. Properties of light transfer

At the drift ice sites, the net incoming power irradiance ranged from 38 to 159 W m^{-2} (band 320—950 nm) above ice during the measurements in 2016. Fig. 5 illustrates the spectral distribution of the downwelling irradiance above ice, under ice and snow, and under bare ice after removing the snow. At the fast ice sites, during the measurements in 2017, the net incoming quantum PAR irradiance ranged from 165 to 369 μmol s^{-1} m^{-2} above ice. The solar altitude was about 18—20° at noon at measurement sites. There was total cloud cover during all these sampling occasions, thus, generally, diffuse downwelling irradiance could be assumed.

3.4.1. Light transfer at drift ice sites

The PAR reflectance of natural snow cover on drift ice ranged from 60%—76% (Table 2). After manually removing the snow, it ranged from 30%—70%. The reflectance of the natural snow cover was on average 1.4 times higher than the reflectance of the surface after removing the snow. There

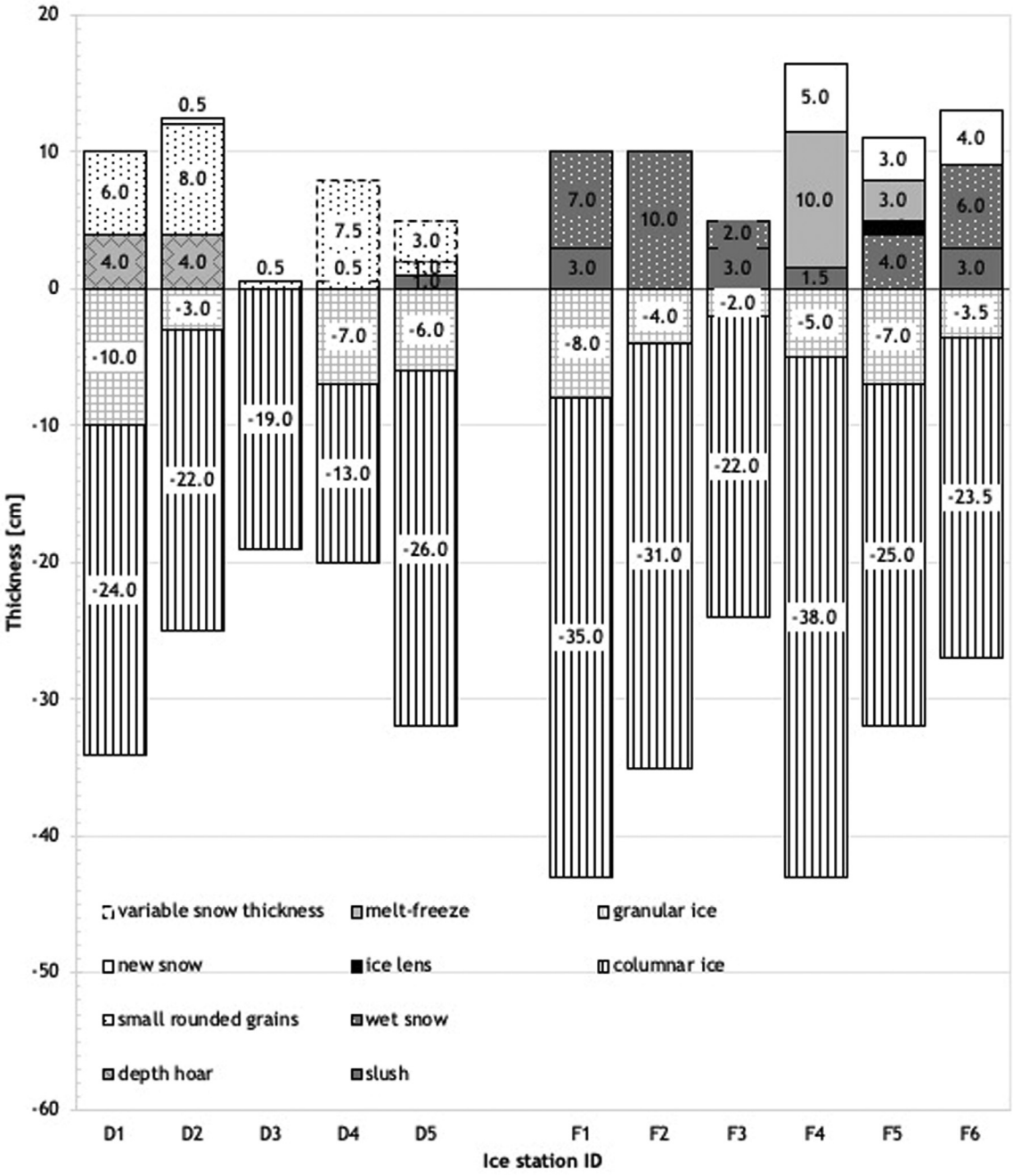

Figure 3 Schematic of the ice and snow structure at drift ice sites (D1—D5) and at fast ice sites (F1—F6). The ice structure was visually characterized into opaque granular ice and clear columnar ice precisely on site with the irradiance measurements. The baseline is the snow-ice-interface as there are no freeboard data available.

was no clear wavelength-dependency over the band 320—900 nm in the reflectance of snow cover (Fig. 6a). At station D1 reflectance without snow was more than twice compared to reflectance at sites D3—D5 (no data at D2, Fig. 6b). The lowest reflectance was measured at D3 above bare ice, where the ice surface was very smooth and the snow could be easily removed. Contrasting snow conditions occurred at D1 and D2, where it was very challenging to remove the snow. Due to incomplete surface reflectance measurements at D1 and D2, the following assumptions were made based on the surface properties. At D1, the reflectance of snow was estimated to be similar to the reflectance spectra at D2. At D2, the reflectance measurement without snow was not available and as adhesion was similar as observed at D1, the reflectance without snow was assumed to be the same as at D1 (without snow) (Table 2).

Transmittance through snow-covered ice was mostly limited by the presence of snow (Table 2). The PAR transmittance was on average only 1.6% at D1 and D2 due to a thicker snow cover while at D3—D5 the PAR transmittance was on average 21%. After removing the snow cover, the PAR transmittance increased on average about three times (from 13%

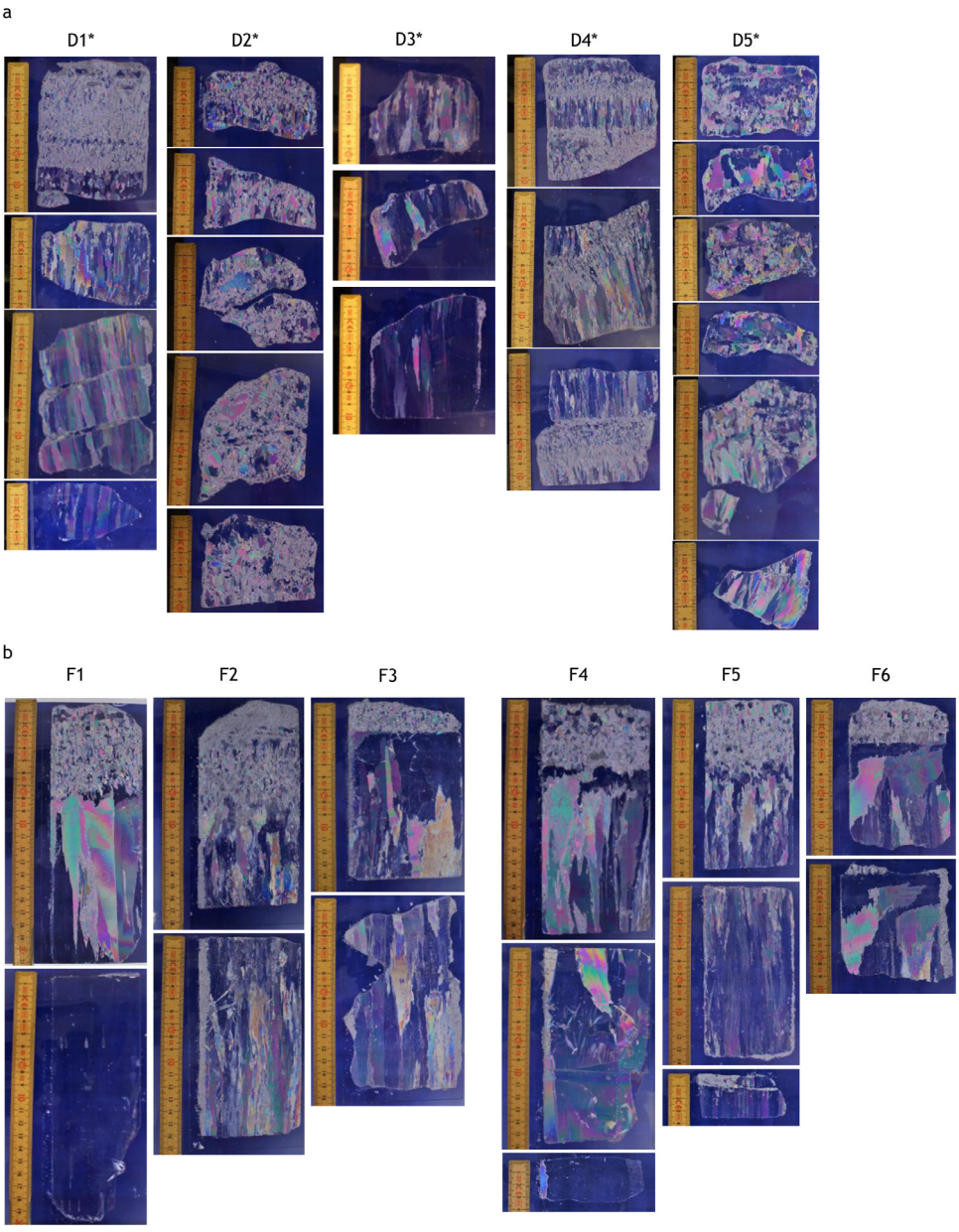

Figure 4 Photographs of the thin sections of ice samples at drift ice sites (D1–D5) and at fast ice sites (F1–F6). At drift ice sites marked with *, the ice core samples were not taken exactly at the point of the irradiance measurements (but within meters).

to 36%). The highest transmittance through bare ice (57%) was measured at D3 with a purely columnar ice structure. Spectral transmittance showed a similar shape, both with and without snow cover. The highest transmittance occurred between 569–582 nm through snow and ice and between 549–585 nm through bare sea ice.

In the presence of snow cover the total PAR diffuse attenuation coefficient, $K_{d,tot}(PAR)$, was on average 4.5 m^{-1}. After removing the snow cover $K_{d,ice}(PAR)$ was 2.5 m^{-1}, i.e. the attenuation was 1.8 times lower without snow (Table 2). $K_d(PAR)$ through ice (both with and without snow) was used to estimate the diffuse attenuation coefficient for snow at each station (Eq. 3). The diffuse attenuation coefficient for snow was $K_{d,snow}(PAR) = 15.7$ m^{-1} (Table 3). The optical thickness of ice and snow was therefore 40 cm and 6.4 cm, respectively, illustrating the strong dependency of light transfer on snow cover thickness. As for the transmittance, the spectral diffuse attenuation coefficient, K_d, showed a clear wavelength dependence (Fig. 7). The minima of the $K_{d,tot}$ (with snow cover) were found in the green (569–588 nm) (Fig. 7a), shifting slightly towards the yellow (569–621 nm) without snow (Fig. 7b). Fig. 8 summarizes the spectral measurements showing the split of incident radiation into reflectance, absorption by ice and snow, and transmittance. When ice is covered by snow, most of the downwelling irradiance (60%) is reflected at the surface. The reflectance is lower for bare ice (40%), and the ice absorption increases in the shorter and longer wavelengths. The site-averaged transmittance was thus highest at 572 nm, both with and without snow cover.

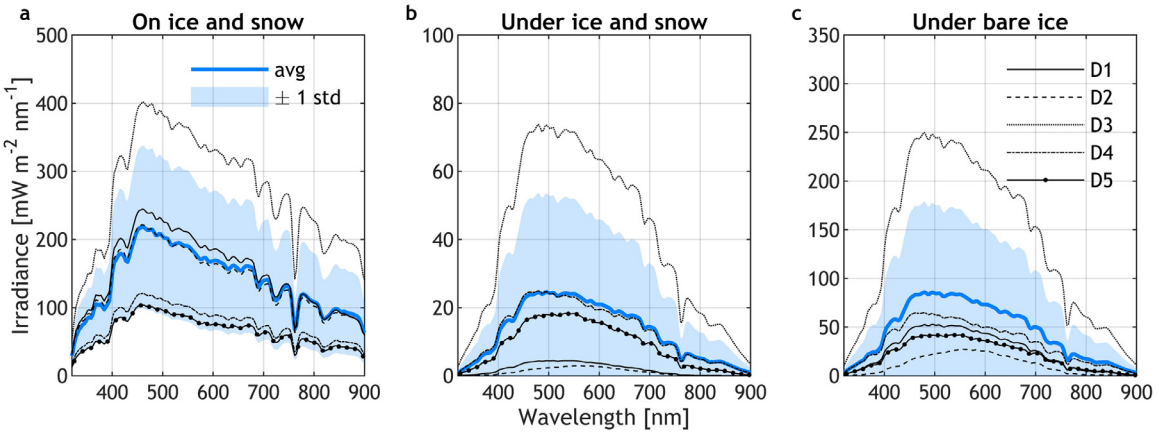

Figure 5 Spectral downwelling irradiance above ice (a), under ice and snow (b) and under bare ice (c) after removing the snow at each station (D1–D5) and their average (blue line) and ±1 standard deviation (blue shaded area). Note the varying scale of the vertical axes.

Table 2 Overview of the snow and ice stratigraphy and measurement of light transfer. First, the thickness of each layer: snow, opaque granular, and clear columnar ice, at the points of irradiance measurements. Then, reflectance, transmittance and diffuse attenuation coefficient (K_d) in PAR band of ice with natural snow cover (column *total*) and snow manually removed (column *no snow*).

Station	Date	Thickness [cm]			Reflectance (*PAR*)		Transmittance (*PAR*) [%]		K_d (*PAR*) [m^{-1}]	
		snow	*granular*	*columnar*	*total*	*no snow*	*total*	*no snow*	*total*	*no snow*
D1	04/03/2016	10	10	24	0.76*	0.70	1.9	26.1	6.9	0.4
D2	05/03/2016	12	3	22	0.76	0.7*	1.2	9.7	8.2	7.9
D3	06/03/2016	1	0	19	0.62	0.30	19.7	57.2	3.3	1.1
D4	07/03/2016	4	7	13	0.63	0.31	22.8	51.7	2.0	1.5
D5	08/03/2016	4	6	26	0.60	0.36	19.6	37.0	2.0	1.7
Mean		*6.2*	*5.2*	*20.8*	*0.67*	*0.47*	*13.0*	*36.3*	*4.5*	*2.5*
F1	01/03/2017	10	8	35	0.5*	0.3*	0.1	8.4	11.2	4.9
F2	01/03/2017	10	4	31	0.5*	0.3*	0.8	13.0	9.3	4.8
F3	01/03/2017	5	2	22	0.5*	0.3*	2.6	21.4	10.2	4.9
F4	03/03/2017	17	5	38	0.85*	0.3*	0.2	8.0	6.9	5.0
F5	03/03/2017	11	7	25	0.85*	0.3*	0.0	13.1	11.3	5.2
F6	03/03/2017	13	4	24	0.85*	0.2*	0.0	16.5	10.5	6.3
Mean		*10.9*	*4.9*	*29.1*	*0.68*	*0.28*	*0.6*	*13.4*	*9.9*	*5.2*

*values estimated from literature, see section 3.3 for details.

Table 3 Diffuse attenuation coefficient for snow, $K_{d,snow}(PAR)$ for drift ice and fast ice sites separately: p-value, coefficient of determination – R^2, standard error – *SE*, standard deviation – *SD*, and sample size – *n*.

	$K_{d,\,snow}(PAR)$	p-value	R^2	SE	SD	n
Drift ice	15.7	0.037	0.70	5.1	11.4	5
Fast ice	21.9	0.003	0.85	4.1	10.0	6

The ratio between power irradiance and quantum irradiance was evaluated from the measurements (Eq. 4). The ratio was 4.5 ± 0.02 μmol J^{-1} above ice and slightly higher under the ice, 4.6 ± 0.05 μmol J^{-1}. Under the ice, the ratio did not change much after removing the snow and the overall statistics were the same with and without snow.

3.4.2. Light transfer at fast ice sites

Surface reflectance was assumed based on visual evaluation and using literature sources as follows: 0.5 for wet snow (stations F1–F3), 0.85 for fresh snow (stations F4–F6), 0.3 for wet ice (stations F1–F5), and 0.2 when sea water had flooded onto the ice surface (F6) (Arst et al., 2006; Leppäranta, 2015; Rasmus et al., 2002). PAR transmittance through snow and ice was very low, on average 0.6%. After removing the snow, the average transmittance about 22-fold, to an average of 13.4%. The lowest transmittances through bare ice were measured at sites F1 and F4 (8.4% and 8.0%, respectively). At these sites, the ice was the thickest with 8 cm granular ice and 35 cm columnar ice at F1 and 5 cm granular ice and 38 cm columnar ice at F4.

$K_{d,tot}(PAR)$ of snow and ice was on average 9.9 m^{-1} and after removing the snow, $K_{d,ice}(PAR)$ was 5.2 m^{-1} (Table 2). The highest $K_{d,tot}(PAR)$ was measured at F5 (11.3 m^{-1}) and $K_{d,tot}(PAR)$ was also high at F1, F3, and F6, where the snow

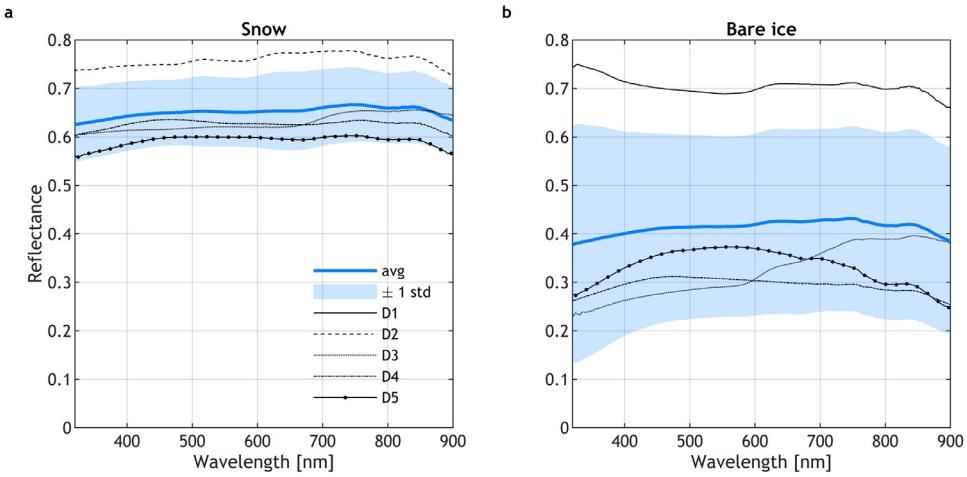

Figure 6 Reflectance of snow cover (a) and bare ice (b) at drift ice stations, their average (blue line) and ±1 standard deviation (blue shaded area). Reflectance of snow cover at D1 and of bare ice at D2 are missing due to incomplete measurements of upwelling irradiance.

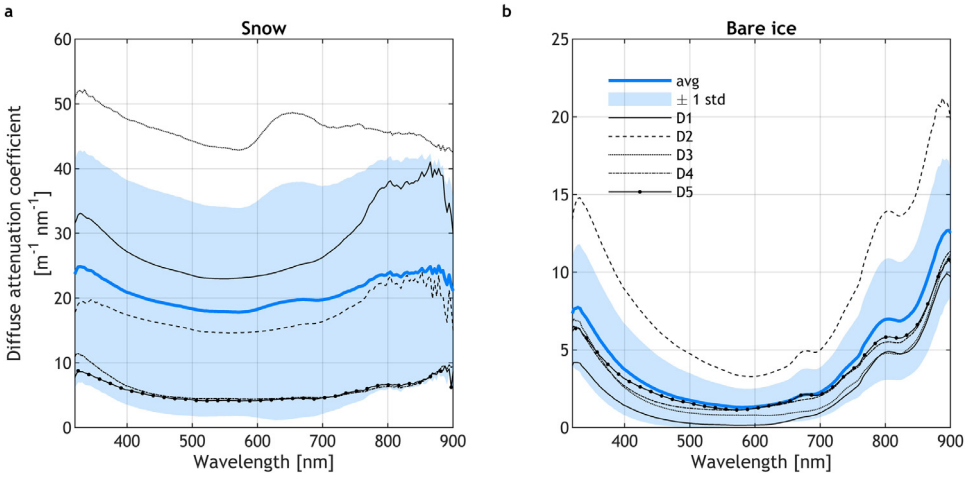

Figure 7 Spectral diffuse attenuation coefficient K_d of snow (a) and bare ice (b) at drift ice stations, their average (blue line) and ±1 standard deviation (blue shaded area). Note the varying scale of the vertical axes.

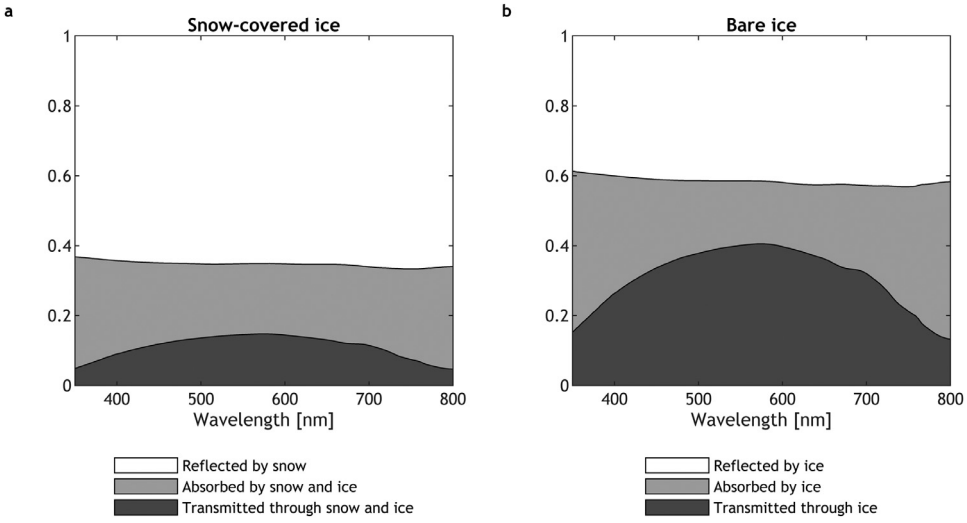

Figure 8 Averaged partitioning of solar radiation at drift ice stations with snow cover (a) and in the case of bare ice (b). Reflectance and transmittance are measured spectra, while absorbed fraction is their residual: $R + A + T = 1$.

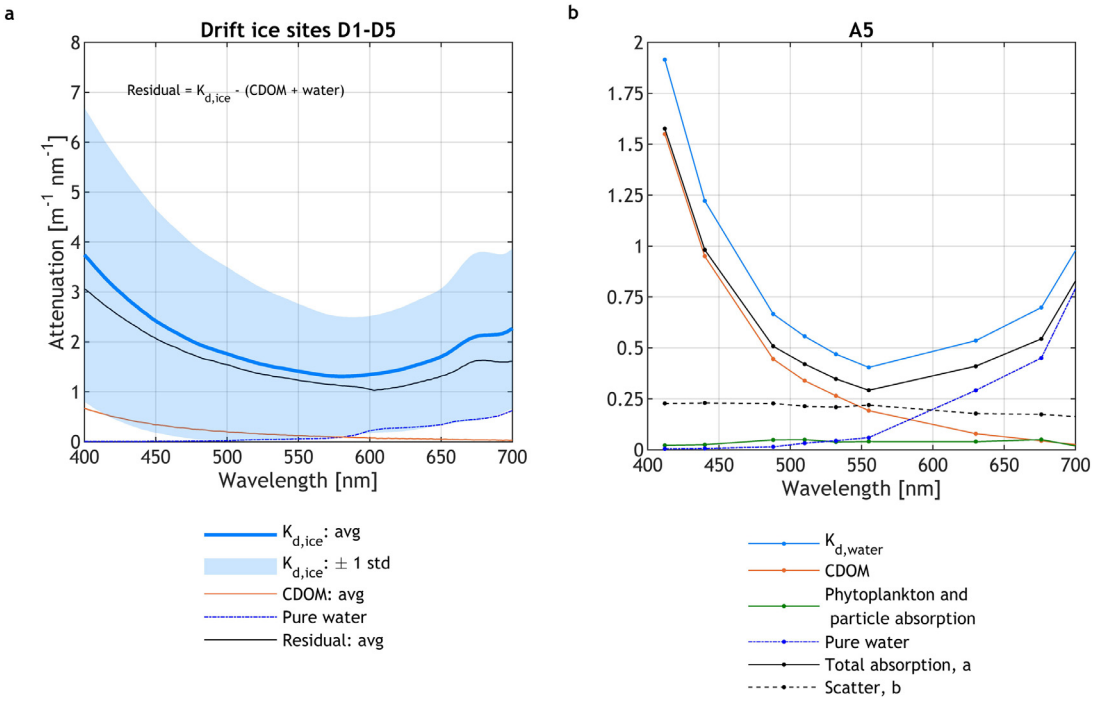

Figure 9 a) Composition of attenuation spectra at drift ice stations showing measured bare ice diffuse attenuation (light blue) against CDOM absorption (orange), pure water absorption (dark blue) (Pope and Fry, 1997) and their residual (black). Solid lines indicate average over the drift ice stations and shaded areas ±1 standard deviation. The full spectra of $K_{d,ice}$ for each station are shown in Figure 7b. b) CDOM absorption (orange), phytoplankton and particle absorption (green), pure water absorption (dark blue) (Pope and Fry, 1997), total absorption *a* (black solid line), particle scatter *b* (black dashed line), and spectral diffuse attenuation coefficient K_d (blue) derived from AC9 measurements in the surface water at station A5, central Bothnian Bay (sea water temperature 1.1°C, CDOM (g_{440}): 0.89 m^{-1}, Chl-*a*: 0.7 μg l^{-1}, $K_d(PAR) = 0.42$ m^{-1}). Note the varying scale of the vertical axes.

was wet with a layer of slush. $K_{d,tot}(PAR)$ and $K_{d,ice}(PAR)$ were also used here to calculate the diffuse attenuation coefficients for snow cover separately. The calculated diffuse attenuation coefficient for snow was $K_{d,snow}(PAR) = 21.9$ m^{-1} (Table 3). Overall, $K_{d,ice}(PAR)$, i.e. without snow, was higher at the fast ice stations compared to drift ice stations.

3.5. Bio-optical substances in sea ice and in surface water

In addition to the ice crystals themselves, the light transfer through the ice and snow also depends on optically active inclusions: gas pockets and bio-optical substances (Chl-*a*, SPM, CDOM). The gas content was only examined qualitatively at site and from photographs of thick sections. The concentrations of bio-optical substances as well as bulk salinity were determined in the laboratory (Table 1) from melted ice samples and water samples from just below the ice (Table 4). Fig. 9 shows the composition of the measured attenuation, absorption and scattering spectra. In Figure 9a, the measured diffuse attenuation coefficient, K_d, and CDOM absorption spectrum are plotted together with the pure water absorption spectrum (Pope and Fry, 1997) as well as their residual: $K_{d,ice} - (CDOM + water)$. The residual illustrates the shape of the attenuation spectra without the influence of CDOM and pure water absorption. CDOM absorbs strongly in the short wavelengths, while pure water absorbs in the long wavelengths. The total absorption and scatter spectra derived from the open water station A5 clearly show that the total absorption is almost entirely dominated by CDOM while water absorbs strongly in the red (Fig. 9b). In surface water, the absorption of phytoplankton in the red part of the spectrum (measured at 676 nm) is hardly detectable. Phytoplankton and particle scatter overall increase the light attenuation within the PAR range, and the effect decreases slightly with increasing wavelength.

At the drift ice sites, Chl-*a* concentrations were generally higher in the melted ice samples than in the water: within the ice Chl-*a* concentrations ranged from 0.8 to 14.1 μg l^{-1}, while in the underlying water concentrations were relatively low, at most 0.5 μg l^{-1} (Table 4). At D2 and D5, a clear attenuation peak was visible between 660–690 nm, indicating the *in vivo* absorption peak of Chl-*a* in the red. At the fast ice sites, the Chl-*a* concentrations in the ice and underlying water did not differ from each other as much, the average Chl-*a* concentration was 1.9 μg l^{-1} both in the melted ice and in the water (Table 4). A comparison between drift ice sites and fast ice sites shows that Chl-*a* concentrations in ice were clearly higher at drift ice sites than at fast ice sites. However, the opposite was observed in the Chl-*a* concentrations in the water with lower values at drift ice sites than at fast ice sites.

The SPM concentrations ranged from 0.6 to 11.9 g m^{-3} for melted ice samples while the range was very small in the water samples: 0.2 to 0.7 g m^{-3} at drift ice sites (Table 4). On average SPM concentrations in ice samples were ten times higher than in the water samples. An ex-

Table 4 Overview of bulk salinity and the bio-optical properties within melted *ice* samples and just below ice in underlying *water*. Bulk salinity from melted *ice* samples and averaged over upper 1 m layer for underlying *water*.

Station	Date	Salinity [g kg^{-1}]		Chl-*a* [μg l^{-1}]		g_{440} [m^{-1}]		SPM [g m^{-3}]		Proportion of inorganic SPM [%]	
		ice (*bulk*)	*water* (*1 m*)	*ice*	*water*	*ice*	*water*	*ice*	*water*	*ice*	*water*
D1	4/3/2016	0.7	3.0	1.7	0.4	0.43	1.19	1.6	0.7	16	46
D2	5/3/2016	0.5	3.1	9.3	0.4	0.34	1.11	11.9	0.4	66	40
D3	6/3/2016	0.6	3.1	5.5	0.4	0.39	1.27	2.9	0.4	57	45
D4	7/3/2016	0.6	3.1	0.8	0.5	0.47	0.92	0.6	0.4	44	31
D5	8/3/2016	0.8	3.0	14.1	0.4	0.34	0.99	3.2	0.2	45	32
Mean		*0.7*	*3.0*	*6.3*	*0.4*	*0.4*	*1.1*	*4.0*	*0.4*	*46.0*	*38.9*
F1	1/3/2017	0.1	4.1	1.2	1.1	0.82	7.37	3.0	1.5	19	26
F2	1/3/2017	0.4	4.8	3.5	3.4	0.53	1.05	1.6	1.3	18	21
F3	1/3/2017	0.7	4.4	1.8	1.7	0.48	0.77	2.1	0.6	19	36
F4	3/3/2017	0.0	3.7	0.6	1.2	1.00	6.55	3.4	3.2	30	24
F5	3/3/2017	0.6	4.9	2.7	1.6	0.67	0.79	2.1	1.0	29	43
F6	3/3/2017	0.7	5.1	1.5	2.1	0.36	1.37	1.3	2.2	26	30
Mean		*0.4*	*4.5*	*1.9*	*1.9*	*0.6*	*3.0*	*2.3*	*1.6*	*23.6*	*29.9*

ceptionally high SPM value for ice samples occurred at D2 with 11.9 g m^{-3}. At this station Chl-*a* was also relatively high (9.3 μg l^{-1}), corresponding well to the observed Chl-*a* absorption peak (660–690 nm) (Fig. 7). At the fast ice sites, the SPM concentration ranged from 1.3 to 3.0 g m^{-3} for the ice samples and from 0.6 to 3.2 g m^{-3} for the water samples (Table 4). Overall, SPM concentrations were higher in the ice samples than in the water samples and differences between ice and water samples were greater at drift than at fast ice sites, similar to Chl-*a* concentrations. The proportions of inorganic SPM varied more within drift ice (16–66%) than within fast ice (18–30%), while in the water the range was similar at both sites, 31–46% at drift ice sites and 21–43% at fast ice sites (Table 4). However, the proportion of inorganic SPM did not show a clear pattern between ice and water samples. At some stations (D2–D5, F4), the proportion was higher in ice than in water, while at other stations (D1, F1–F3, F5, F6) the opposite was true.

At drift ice sites, CDOM absorption, g_{440}, varied only little both in the ice samples (0.34–0.47 m^{-1}) and in the water samples (0.92–1.27 m^{-1}). CDOM absorption was on average three times lower in ice than in water, indicating CDOM rejection during freezing. This is the opposite behaviour to what is observed for Chl-*a* and SPM. At fast ice sites, CDOM absorption had a larger range for melted ice samples (0.36–1.00 m^{-1}) and even larger for the underlying water (0.77–7.37 m^{-1}). The large range in the underlying water confirms the observed river plume. At F1 and F4, closest to the shore, the CDOM absorption was highest, both in the ice and in the water. Here, the CDOM absorption was six to nine times higher in the underlying water, while within the ice CDOM absorption was at the most twice as high. CDOM absorption was lower in ice than in water at all stations, and this difference was even more obvious in fast ice than in drift ice (Table 4). The rejection of CDOM from the ice varied much more at the fast ice sites than at the drift ice sites. At the fast ice sites, CDOM absorption in the meltwater was 22 $\pm$ 29% of the CDOM absorption in the underlying water, while at the drift ice sites, CDOM absorption in melted ice samples was 36 $\pm$ 8% of the CDOM absorption in the underlying water.

The transmittance through bare ice was lowest at F1 (8.4%) and F4 (8%). These coastal stations had high amounts of CDOM and SPM both in the ice and the underlying water originating from the river discharge and thus leading to an increase of light attenuation within the ice. Transmittance was also low at D2 (9.7%) with high SPM concentration in ice (11.9 g m^{-3}), contributing to the low transmittance. In fast ice, CDOM absorption and concentration of SPM were higher than in the drift ice, presumably reducing the light transfer through the ice cover.

In order to compare CDOM absorption with salinity concentration, the bulk salinity was determined for melted ice samples and in the upper 1 m layer of the underlying water column. The salinity of ice was very stable: 0.6 ppt and 0.7 ppt in drift ice and fast ice, respectively. The same was true for the water salinity in the upper 1 m, but values differed slightly from one another: on average 3.0 ppt at the drift ice sites and 4.5 ppt at the fast ice sites. Similar to sea water, an inverse correlation between CDOM and salinity was found within the ice, the lower the bulk salinity the higher the CDOM absorption (g_{440}). However, within the ice the ratio of CDOM absorption to salinity was higher than in the underlying water. The rejection of both CDOM and salinity was more efficient at fast ice sites, the CDOM in ice was on average 22% and salinity 9% of the underlying water. While in drift ice, CDOM was 36% and salinity 21% of the underlying water.

4. Discussion

Drift ice and fast ice properties and the light transfer through different types of snow and ice cover were studied during two consecutive springs, in 2016 and 2017. In addition, salinity and concentrations of bio-optical substances were studied both within the ice and in the underlying water. The fast ice structure was typical for coastal sea ice with a granular upper layer and a columnar lower layer, while the drift ice had a more complex structure. Drift ice is characterized by spatial variability in thickness and structure, due to the dynamics of the ice field and processes such as rafting and ridging as well as seawater flooding and seawater being trapped between ice floes. Differences in ice structure between drift ice and fast ice confirm that the growth history of drift ice is considerably more dynamic than for the coastal fast ice.

A strong freshwater input transports high concentrations of humic substances to the Baltic Sea, especially to its northernmost parts the Bothnian Sea and the Bothnian Bay. CDOM absorption, g_{440}, has been found to be inversely related to salinity in the Baltic Sea (Harvey et al., 2015; Kari et al., 2018; Kowalczuk et al., 2006; Kratzer et al., 2003). We found similar relationships for ice: the lower the bulk salinity the higher the CDOM absorption. However, in ice the ratio of CDOM absorption to salinity was higher than in the underlying water. Müller et al. (2011) found a similar enrichment of CDOM in sea ice. They suggested that the enrichment is caused by the initial freezing process and also by the aggregation of CDOM within the brine. The rejection of both CDOM and salinity was more efficient at the fast ice sites, where also both the CDOM absorption and salinity in the parent sea water were higher than at the drift ice sites.

In order to give a thorough statistical analysis, an increased number of samples would be useful. Due to the limited number of data points (n = 11), it was challenging to examine the main or at least significant patterns, as to how bio-optical substances affect the light transfer through the ice cover. The SPM concentration had a positive significant effect on the diffuse attenuation coefficient ($p < 0.001$) at drift ice sites, but when D2 (with comparatively high concentration) was removed, there was no statistically significant effect. Neither SPM nor the other bio-optical substances were shown to affect the light attenuation or transmittance in a statistically significant manner. The lack of quantitative data of gas content hides weaker signals and casts uncertainty onto the results. In order to evaluate the influence of ice structure on light transfer through ice, it is important to note that at the drift ice sites the layer thicknesses were determined visually and measured at site (Fig. 3). Also, the samples for the analysis of the bio-optical substances were collected on site. The ice cores for the ice structure analysis (Fig. 4), however, were not taken exactly at the point of the irradiance measurements (but within metres) at the drift ice sites. Despite these limitations, this

study provides a unique dataset as it compares drift ice and fast ice properties in combination with bio-optical substances.

In contrast to the planar irradiance measurements at drift ice sites, irradiance measurements were performed with a scalar irradiance instrument at the fast ice sites. In order to compare these measurements, we utilised the ratio of planar to scalar irradiance. The ratio was estimated based on a study by Arst et al. (2006), who measured the ratio under ice-covered waters. In their study, the ratio of planar to scalar irradiance (averaged over the upper 2 m layer) ranged from 0.39 to 0.76, depending on the optical quality of the water body, ranging from hypereutrophic to oligotrophic water bodies. The ratio was found to increase with depth under snow and ice cover. Here, 0.5 was selected to represent the ratio just below the ice cover. As the ratio differs between water bodies, the selection of the ratio may cause a difference of −6.8% to +21% in the calculated transmittance. Selecting minimum and maximum ratios would cause a range from 9.4 m^{-1} to 10.0 m^{-1} in the mean $K_{d,tot}(PAR)$ and from 4.6 m^{-1} to 5.4 m^{-1} in the mean $K_{d,ice}(PAR)$.

The ratio between the power irradiance and quantum irradiance, q_{PAR}/E_{PAR}, allows for the irradiance data to be converted to the same units and also describes the variation of the spectral distribution of the irradiance. Here, q_{PAR}/E_{PAR} was slightly lower on the surface above ice $q_{PAR}/E_{PAR} = 4.5$ μmol J^{-1} than the theoretical value for white light (4.6 μmol J^{-1}) indicating more irradiance in the short wavelengths compared to white light. Under ice, the ratio was higher, $q_{PAR}/E_{PAR} = 4.6$ μmol J^{-1}, whether there was snow or not. The highest value, $q_{PAR}/E_{PAR} = 4.7$ μmol J^{-1}, was observed at D2 where transmittance was lowest (9.7%). The q_{PAR}/E_{PAR} higher than for white light indicates more irradiance at longer wavelengths compared to white light. Below ice, the light spectrum is modified and typically $q_{PAR}/E_{PAR} > 4.6$ μmol J^{-1} (Reinart et al., 1998). Reinart et al. (1998) found that the q_{PAR}/E_{PAR} ratio in lake waters depends on the depth and transparency of the water. The q_{PAR}/E_{PAR} ratio ranged here from 4.7–5.8 μmol J^{-1}.

Surface reflectance is very sensitive to the properties of the surface. At drift ice sites, surface reflectance of the natural snow cover ranged from 0.60 to 0.76 and after removing the snow it was on average 1.4 times lower. This result confirms the dominant role of snow cover on surface reflectance. At the fast ice sites, literature data (Arst et al., 2006; Leppäranta, 2015; Rasmus et al., 2002) were employed to evaluate the PAR reflectance since no reflectance measurements were available. Surface reflectance was assumed to be 0.5 for wet snow, 0.85 for fresh snow, 0.3 for wet ice, and 0.2 when sea water had flooded onto the ice surface. After removing the snow, clear, level ice with only a columnar ice structure had the lowest measured reflectance (0.31), while the ice surface with opaque ice and snow adhered to the surface had the highest reflectance (0.70) due to higher surface scatter. These reflectance measurements fall in the same range as found in previous investigations of fast ice in the Gulf of Finland, where the reflectance of snow cover ranged from 0.42 to 0.76 and from 0.30 to 0.38 without snow (Rasmus et al., 2002).

Transmittance was mostly affected by the snow thickness and type. The optical thickness of snow and ice were 6.4 cm and 40 cm, respectively, and regarding the thickness variations, the high sensitivity of transmittance to snow becomes obvious. Snow cover behaves like a grey light filter changing the spectral shape only slightly. The maximum transmittance through the snow-covered ice was found at 569–582 nm and for bare ice at 548–585 nm. The maximum transmittance of bare ice is similar as of water and bare ice thus might not be detected by optical remote sensing data processors, but could be misinterpreted as surface water instead. This may lead to the detection of erroneously high Chl-*a* concentrations in surface waters (Beltrán-Abaunza et al., 2016).

At fast ice sites, the snow cover was mostly wet snow, which absorbs most of the solar radiation. Thus, transmittance through snow and ice was very low. Earlier studies on light transfer through brackish sea ice in the coastal landfast ice zone in the Gulf of Finland were all conducted in Santala Bay. This needs to be accounted for when comparing the results, since only a small variability of stations is considered due to few available studies. The transmittance results are comparable to previous studies in the fast ice zone in Santala Bay, where the PAR transmittance was 13.6% with 3 cm snow on the ice (Rasmus et al., 2002), and 15% with wet snow patches and 52% for clear ice (Leppäranta et al., 2003). In a study by Ehn et al. (2004) on melting fast ice, the PAR transmittance ranged from 25% to 42%. Rasmus et al. (2002) measured the highest transmittance at 556 nm and Ehn et al. (2004) between 550 and 660 nm. In Arctic sea ice, the maximum transmittance is at 470 nm (blue) (Perovich et al., 1998), but CDOM and Chl-*a* absorption cause a shift in the maximum transmittance towards the green (Arrigo et al., 1991; Kauko et al., 2017). Kauko et al. (2017) measured highest transmittance at 558 nm in a refrozen lead in Arctic sea ice, which corresponds well with the transmittance spectra of Baltic Sea ice.

At fast ice sites the diffuse attenuation coefficient, $K_{d,ice}(PAR)$, was on average 5.2 m^{-1} while at drift ice sites $K_{d,ice}(PAR)$ was on average 2.5 m^{-1} with a more complex, multi-layered ice structure. These results are in agreement with previous studies. Rasmus et al. (2002) measured 6.8 m^{-1}, while in the study by Arst et al. (2006) $K_{d,ice}(PAR)$ ranged from 1.5 to 5.5 m^{-1} (mean 3.2 m^{-1}) in fast ice in the Gulf of Finland. An attempt was made to include a three-layer diffuse attenuation coefficient with separate snow, snow-ice, and congelation ice layers with inconclusive results. The estimates of the diffuse attenuation coefficients for snow were 15.7 m^{-1} at drift ice and 21.9 m^{-1} at fast ice sites which is in the correct order of magnitude. The higher values at the fast ice sites can be explained by the higher liquid water content in snow. Järvinen and Leppäranta (2011) studied the transmission of solar radiation through snow cover and measured the diffuse attenuation coefficient in two layers inside the snowpack, 0–4 cm and 4–8 cm. In their study, the attenuation coefficients varied between 4.0 m^{-1} and 13.0 m^{-1}.

The spectral diffuse attenuation coefficient, K_d, showed minimum values in the wavelength range 569–621 nm, corresponding to the maximum range of transmittance, both with and without snow cover. However, after removing

the snow, the minimum $K_{d,ice}$ decreased from 3.7 m^{-1} to 1.3 m^{-1} (mean of the minima $K_{d,ice}$ at the drift ice sites). At D2 and D5, clear attenuation Chl-*a* peaks were visible between 660–690 nm, these stations had the highest concentrations of Chl-*a*: 9.3 $\mu g\ l^{-1}$ at D2 and 14.1 $\mu g\ l^{-1}$ at D5. As the highest measured bulk salinity (0.8 ppt) at D5 suggests, an increased Chl-*a* concentration may imply an increased brine volume as the brine may serve as a habitat for phytoplankton (Huttunen and Niemi, 1986; Ikävalko, 1998; Ikävalko et al., 1994). The high Chl-*a* and SPM concentrations at D2 may have caused the rather low transmittance (9.7%) and high diffuse attenuation coefficient for ice $K_{d,ice}(PAR)$ (7.9 m^{-1}). Concentrations of Chl-*a* and SPM varied among the sampling sites, but the concentrations were generally higher at the drift ice sites than at the fast ice sites. The high concentration of SPM (including phytoplankton) was presumably caused by the dynamics of the drift ice field. The ice floes may have trapped sea water, including the substances within, during ice breakage and deformation processes. Additional attenuation measurements were collected in the surface water in the central Bothnian Bay in May 2018, just after the ice melting. The results confirm that in surface waters the total absorption is almost entirely dominated by CDOM in the short wavelengths, while water absorbs strongly in the longer wavelengths. The residual of $K_{d,ice}$, CDOM, and pure water absorption should correspond to white scatter caused by gas inclusions inside the sea ice. Our results show, however, a clear wavelength-dependency with increasing attenuation towards lower wavelengths and a peak at 660–690 nm which corresponds to the phytoplankton absorption peak. The spectral shape of the K_d is overall dominated by the spectral absorption of CDOM and of pure water.

When comparing the spectral K_d of ice (Fig. 9a) to the one of sea water (Fig. 9b) one can see that the spectral shape is similar but the ice has a much stronger overall attenuation. This is mostly caused by the white scatter of gas inclusion in the ice, increasing the total attenuation spectrum. Additionally, particulate matter included in the ice (Table 4) may add to the scatter. Figure 9b illustrates the spectral slope of scatter in water that slightly decreases from 400 to 700 nm. The main effect, however, is also to shift the total K_d spectrum up to a higher level whilst the spectral absorption of particles and phytoplankton combined is relatively low in this example due to generally low concentrations. In Figure 9a, however, the average K_d shows a clear peak in the red, caused by the extremely high chlorophyll-*a* concentrations in some of the ice melt samples (D2 and D5, see Table 4). It must be noted that spectral K_d is a non-linear function of the absorption and scatter of all optical components (Kirk, 2011), and therefore is not simply additive.

The results shown here are in agreement with those of Uusikivi et al. (2010) who measured the absorption coefficient for CDOM as well as of particulate matter in melted fast ice samples. The high SPM concentration in ice indicates high particulate matter absorption and scatter, which may contribute to the overall high attenuation. In order to develop a full picture of the factors affecting the light transfer and their variability, additional studies will be needed that cover *in situ* measurements of the spectral signature of each bio-optical substance within the ice. However, when measuring the optical properties of melted sea ice, the melting process may influence the concentrations or properties of the bio-optical substances (e.g. Rintala et al., 2014). Seasonal measurements of irradiance inside sea ice would provide valuable additional information with minimum disturbance on the sea ice structure and gas inclusions, e.g. utilising autonomous PAR-sensors (Lei et al., 2011) or fibre optics spectrometry (Wang et al., 2019). A full picture of the light transfer through sea ice and snow cover would provide us with better information about the seasonal changes in the light conditions and light availability under sea ice.

5. Conclusions

Light transfer through the ice and snow cover was studied in the Gulf of Bothnia, northern Baltic Sea. In March 2016, drift ice with multi-layered structure was studied, and in March 2017 the measurements were taken in a landfast ice site where typical coastal sea ice was found with a two-layer structure of granular and columnar ice. An additional study was performed in May 2018 to characterize the effect of CDOM and phytoplankton absorption on the spectral diffuse attenuation coefficient. All study sites were located between 63°N and 66°N. Due to total cloud cover during the field campaigns, the downwelling irradiance could be assumed to be diffuse. Snow cover was the dominant factor influencing the light transfer through sea ice. After manually removing the snow, the transmittance was three times higher at drift ice sites and 22 times higher at fast ice sites. The relation between the power irradiance and quantum irradiance was not affected by the snow cover, indicating that it generally reduces the amount of irradiance under ice but does not markedly change its spectral composition. Strongly scattering gas inclusions in the ice significantly increased the diffuse attenuation coefficient K_d but did not noticeably change the spectral distribution, indicating that they – similar to snow- act as white scatterers. This study presents a unique dataset of bio-optical and physical properties of drift ice and fast ice in the Baltic Sea. Our results confirm the differences in these properties in fast ice and drift ice due to differences both in their growth history and in the properties of their parent sea water. Typical to Baltic Sea, both sea water and sea ice have high concentrations of CDOM and SPM, especially in the vicinity of river outlets. CDOM was found to have a strong effect on the spectral slope of K_d at short wavelengths, while pure water absorbs strongly in the long wavelengths. Generally, the effect of phytoplankton pigments on spectral K_d was hardly detectable, apart from at very high concentrations which lead to an increase of K_d at around 660–690 nm. Thus, bio-optical substances included in the ice increase the light attenuation and alter the spectral distribution of the light transfer through ice. The transmittance through bare ice was lowest at the coastal fast ice sites, where also CDOM absorption and SPM concentration were higher than at the drift ice sites. As our results highlight the critical role of snow cover on the light conditions under ice, we recommend further studies on snow cover properties as well as their temporal and spatial variability, which is also relevant if primary production estimation shall be properly performed.

Acknowledgements

This work was financially supported by the Department of Ecology, Environment and Plant Science at Stockholm University, and by the Swedish National Space Agency [Dnr. 147/12], by Nordforsk [project ref. 80106], and by the German Academic Exchange Service (DAAD) [grant number: 57212311]. Thanks to the marine monitoring group at Umeå University and the Swedish Coast Guards on KBV181 for great support during field work. The Swedish Agency for Water and Marine Management as well as County Board Norrbotten provided financial support via the EU Interreg Nord project SEAmBOTH [contract no. 502-14063-2017]. We are grateful to Dr. Eero Rinne, the chief scientist of the sea ice cruise onboard r/v *Aranda*, for the possibility to join the scientific staff. We want to thank the Finnish Meteorological Institute for the facilities during the research cruise and the scientists at the Finnish Environment Institute for support both in preparations and during the cruise. We also thank professor Jukka Horppila at the Ecosystems and Environment Research Programme, Faculty of Biological Environmental Sciences at the University of Helsinki, Finland, for lending the RAMSES instrument for our field campaign onboard r/v *Aranda*. We thank laboratory technician Kathrin Dietrich at the Institute for Chemistry and Biology of the Marine Environment at the Carl von Ossietzky University of Oldenburg, Germany, for the gravimetrical analysis of the SPM samples collected during the r/v *Aranda* cruise. The access to the facilities at the Umeå Marine Research Centre and the support from the station's staff are gratefully acknowledged, as well as the help by Maija Jauhiainen during the field campaign in Umeå. We thank Stefan Svensson at the Department of Ecology, Environment and Plant Science at Stockholm University, Sweden, for the fast ice salinity measurements.

Supplementary material

Supplementary material associated with this article can be found, in the online version, at doi:10.1016/j.oceano.2020.04.001.

References

Arrigo, K.R., Sullivan, C.W., Kremer, J.N., 1991. A bio-optical model of Antarctic sea ice. J. Geophys. Res. 96 (C6), 10581—10592, https://doi.org/10.1029/91JC00455.

Arst, H., 2003. Optical properties and remote sensing of multicomponental water bodies. Springer Science & Business Media.

Arst, H., Erm, A., Leppäranta, M., Reinart, A., 2006. Radiative characteristics of ice-covered fresh- and brackish-water bodies. Proc. Est. Acad. Sci. Geol. 55, 3—23.

Beltrán-Abaunza, J.M., Kratzer, S., Höglander, H., 2016. Using MERIS data to assess the spatial and temporal variability of phytoplankton in coastal areas. Int. J. Remote Sens. 1—25, https://doi.org/10.1080/01431161.2016.1249307.

Doerffer, R., 2002. Protocols for the validation of MERIS water products — PO-TN-MEL-GS-0043. ESA Publ. 1—46.

Ehn, J., Granskog, M.A., Reinart, A., Erm, A., 2004. Optical properties of melting landfast sea ice and underlying seawater in Santala Bay, Gulf of Finland. J. Geophys. Res. 109. art. no. C09003, 12 pp. https://doi.org/10.1029/2003JC002042 .

Granskog, M.A., Kaartokallio, H., Kuosa, H., Thomas, D.N., Vainio, J., 2006. Sea ice in the Baltic Sea — A review. Estuar. Coast. Shelf Sci. 70, 145—160, https://doi.org/10.1016/j.ecss.2006.06.001.

Harvey, E.T., Kratzer, S., Andersson, A., 2015. Relationships between colored dissolved organic matter and dissolved organic carbon in different coastal gradients of the Baltic Sea. Ambio 44, 392—401, https://doi.org/10.1007/s13280-015-0658-4.

Huttunen, M., Niemi, Å, 1986. Sea-ice algae in the Northern Baltic Sea. Mem. Soc. Fauna Flora Fenn. 62, 58—62.

Ikävalko, J., 1998. Further observations on flagellates within sea ice in northern Bothnian Bay, the Baltic Sea. Polar Biol 19, 323—329, https://doi.org/10.1007/s003000050253.

Ikävalko, J., Kristiansen, J., Thomsen, H.A., 1994. A revision of the taxonomic position of Syncrypta glomerifera (Chrysophyceae), establishment of a new genus Lepidochrysis and observations on the occurrence of *L. glomerifera* comb. nov. in brackish water. Nord. J. Bot 14, 339—344, https://doi.org/10.1111/j.1756-1051.1994.tb00617.x.

Järvinen, O., Leppäranta, M., 2011. Transmission of solar radiation through the snow cover on floating ice. J. Glaciol. 57, 861—870, https://doi.org/10.3189/002214311798043843.

Kari, E., Kratzer, S., Beltrán-Abaunza, J.M., Harvey, E.T., Vaičiūtė, D., 2016. Retrieval of suspended particulate matter from turbidity — model development, validation, and application to MERIS data over the Baltic Sea. Int. J. Remote Sens. 38, 1—21, https://doi.org/10.1080/01431161.2016.1230289.

Kari, E., Merkouriadi, I., Walve, J., Leppäranta, M., Kratzer, S., 2018. Development of under-ice stratification in Himmerfjärden bay, north-western Baltic proper, and their effect on the phytoplankton spring bloom. J. Mar. Sci. 186, 85—95, https://doi.org/10.1016/j.jmarsys.2018.06.004.

Kauko, H.M., Taskjelle, T., Assmy, P., Pavlov, A.K., Mundy, C.J., Duarte, P., Fernández-Méndez, M., Olsen, L.M., Hudson, S.R., Johnsen, G., Elliott, A., Wang, F., Granskog, M.A., 2017. Windows in Arctic sea ice: Light transmission and ice algae in a refrozen lead. J. Geophys. Res. Ocean 1486—1505, https://doi.org/10.1002/2016JG003626.

Kawamura, T., Shirasawa, K., Ishikawa, N., Lindfors, A., Rasmus, K., Granskog, M.A., Ehn, J., Leppäranta, M., Martma, T., Vaikmäe, R., 2001. Time-series observations of the structure and properties of brackish ice in the Gulf of Finland. Ann. Glaciol. 33, 1—4, https://doi.org/10.3189/172756401781818950.

Kirk, J.T.O., 2011. Light and photosynthesis in aquatic ecosystems, 3rd edn Cambridge Univ. Press, Cambridge, United Kingdom 662 pp.

Kowalczuk, P., Stedmon, C.A., Markager, S., 2006. Modeling absorption by CDOM in the Baltic Sea from season, salinity and chlorophyll. Mar. Chem. 101, 1—11, https://doi.org/10.1016/j.marchem.2005.12.005.

Kratzer, S., 2000. Bio-optical studies of coastal waters. University of Wales, Bangor Ph.D. thesis.

Kratzer, S., Håkansson, B., Sahlin, C., 2003. Assessing Secchi and photic zone depth in the Baltic Sea from satellite data. Ambio 32, 577—585, https://doi.org/10.1579/0044-7447-32.8.577.

Kratzer, S., Moore, G., 2018. Inherent Optical Properties of the Baltic Sea in Comparison to Other Seas and Oceans. Remote Sens 10, 1—28, https://doi.org/10.3390/rs10030418.

Kratzer, S., Tett, P., 2009. Using bio-optics to investigate the extent of coastal waters: A Swedish case study. Eutrophication in Coastal Ecosystems. Springer, Amsterdam, 169—186.

Lei, R., Leppäranta, M., Erm, A., Jaatinen, E., Pärn, O., 2011. Field investigations of apparent optical properties of ice cover in Finnish and Estonian lakes in winter 2009. Est. J. Earth Sci 60, 50—64, https://doi.org/10.3176/earth.2011.1.05.

Leppäranta, M., 2015. Freezing of lakes and the evolution of their ice cover, 1st edn Springer, Praxis, Cichester, 301 pp., https://doi.org/10.1007/978-3-642-29081-7 .

Leppäranta, M., 2011. The Drift of Sea Ice, 2nd edn. Springer, Praxis, Chichester, 347 pp., https://doi.org/10.1007/978-3-642-04683-4 .

Leppäranta, M., 1983. A growth model for black ice, snow ice and snow thickness in subarctic basins. Hydrol. Res. 14, 59—70, https://doi.org/10.2166/nh.1983.0006.

Leppäranta, M., Myrberg, K., 2009. Physical Oceanography of the Baltic Sea. Springer, Praxis, Chichester, 401 pp., https://doi.org/10.1007/978-3-540-79703-6 .

Leppäranta, M., Reinart, A., Erm, A., Arst, H., Hussainov, M., Sipelgas, L., 2003. Investigation of Ice and Water Properties and Under-ice Light Fields in Fresh and Brackish Water Bodies. Nord. Hydrol. 34, 245—266, https://doi.org/10.2166/nh.2003.0006.

Leppäranta, M., Tikkanen, M., Shemeikka, P., 1998. Observations of Ice and Its Sediments on the Baltic Sea Coast. Hydrol. Res. 29, 199—220.

McDougall, T.J., Barker, P.M., 2011. Getting started with TEOS-10 and the Gibbs Seawater (GSW) Oceanographic Toolbox. SCOR/IAPSO WG127, 28 pp..

Müller, S., Vähätalo, A.V., Granskog, M.A., Autio, R., Kaartokallio, H., 2011. Behaviour of dissolved organic matter during formation of natural and artificially grown Baltic Sea ice. Ann. Glaciol. 52, 233—241, https://doi.org/10.3189/172756411795931886.

Ohde, T., Siegel, H., Gerth, M., 2007. Validation of MERIS Level-2 products in the Baltic Sea, the Namibian coastal area and the Atlantic Ocean. Int. J. Remote Sens. 28, 609—624, https://doi.org/10.1080/01431160600972961.

Palosuo, E., 1963. The Gulf of Bothnia in winter. II Freezing and ice forms, Merentutkimuslaitoksen Julkaisu/ Havsforskningsinstitutets Skrift. Finnish Institute of Marine Research, Helsinki, Finland.

Palosuo, E., 1961. Crystal structure of brackish and freshwater ice. Bull. Int. Assoc. Sci. Hydrol. 54, 9—14.

Parsons, T.R., Maita, Y., Lalli, C.M., 1984. A Manual of Chemical and Biological Methods for Seawater Analysis. Pergamon Press, Oxford 188 pp. https://doi.org/10.1002/iroh.19850700634 .

Perovich, D.K., 1996. The Optical Properties of Sea Ice. In: Leppäranta, M. (Ed.), Physics of Ice-Covered Seas, 1. Univ. Helsinki, Helsinki, 195—230.

Perovich, D.K., Roesler, C.S., Pegau, W.S., 1998. Variability in Arctic sea ice optical properties. J. Geophys. Res. Ocean 103, 1193—1208, https://doi.org/10.1029/97JC01614.

Pierson, D.C., Kratzer, S., Strömbeck, N., Håkansson, B., 2008. Relationship between the attenuation of downwelling irradiance at 490 nm with the attenuation of PAR (400 nm—700 nm) in the Baltic Sea. Remote Sens. Environ. 112, 668—680, https://doi.org/10.1016/j.rse.2007.06.009.

Pope, R.M., Fry, E.S., 1997. Absorption spectrum (380—700 nm) of pure water. II . Integrating cavity measurements. Appl. Opt. 36, 8710—8723.

Rasmus, K., Ehn, J., Granskog, M., Kärkäs, E., Leppäranta, M., Lindfors, A., Pelkonen, A., Rasmus, S., Reinart, A., 2002. Optical Measurements of Sea Ice in the Gulf of Finland. Hydrol. Res. 33, 207—226.

Reinart, A., Arst, H., Blanco-Sequeiros, A., Herlevi, A., 1998. Relation between underwater irradiance and quantum irradiance in dependence on water transparency at different depths in the water bodies. J. Geophys. Res. 103, 7749—7752, https://doi.org/10.1029/97JC03645.

Rintala, J.-M., Piiparinen, J., Blomster, J., Majaneva, M., Müller, S., Uusikivi, J., Autio, R., 2014. Fast direct melting of brackish sea-ice samples results in biologically more accurate results than slow buffered melting. Polar Biol. 1811—1822, https://doi.org/10.1007/s00300-014-1563-1.

Shokr, M., Sinha, N (Eds.), 2015. Laboratory Techniques for Revealing the Structure of Polycrystalline Ice. Sea Ice: Physics and Remote Sensing. Geophys. Monogr. 209, AGU. John Wiley & Sons, Hoboken, 231—269.

Simis, S.G.H., Olsson, J., 2013. Unattended processing of shipborne hyperspectral reflectance measurements. Remote Sens. Environ. 135, 202—212, https://doi.org/10.1016/j.rse.2013.04.001.

Simon, A., Shanmugam, P., 2016. Estimation of the spectral diffuse attenuation coefficient of downwelling irradiance in inland and coastal waters from hyperspectral remote sensing data: Validation with experimental data. Int. J. Appl. Earth Obs. Geoinf. 49, 117—125, https://doi.org/10.1016/j.jag.2016.02.003.

Strickland, J.D.H., Parsons, T.R., 1972. A practical handbook of seawater analysis, 2nd edn. Fisher. Res. Board Canada, Ottawa, Canada, 293 pp., https://doi.org/10.1002/iroh.19700550118 .

Uusikivi, J., Granskog, M.A., Sonninen, E., 2011. Meteoric ice contribution and influence of weather on landfast ice growth in the Gulf of Finland. Baltic Sea. Ann. Glaciol. 52, 91—96, https://doi.org/10.3189/172756411795931796.

Uusikivi, J., Vähätalo, A.V, Granskog, M.a., Sommaruga, R., 2010. Contribution of mycosporine-like amino acids and colored dissolved and particulate matter to sea ice optical properties and ultraviolet attenuation. Limnol. Oceanogr. 55, 703—713, https://doi.org/10.4319/lo.2010.55.2.0703.

Vogt, J., Soille, P., De Jager, A., Rimavči\=ut\.e, E., Mehl, W., Foisneau, S., Bódis, K., Dusart, J., Paracchini, M.L., Haastrup, P., Bamps, C., 2007. A pan-European River and Catchment Database. Rep. EUR 22920 En. [JRC Ref. Rep.], CCM, IES, JCR EU. Office for Official Publ. EU (OPOCE), Luxembourg, 124 pp., https://doi.org/10.2788/35907 .

Wang, H., Nan, L., Han, J., Chen, Y., Huang, H., 2019. Long-term measurement of solar irradiance above, within, and under sea ice in polar environments by using fiber optic spectrometry. J. Atmos. Ocean. Technol. 36, 1773—1787, https://doi.org/10.1175/JTECH-D-19-0086.1.

Weeks, W.F., Ackley, S.F., 1986. The Growth, Structure, and Properties of Sea Ice. In: Untersteiner, N. (Ed.), The Geophysics of Sea Ice. Springer, Boston, 9—164.

Weeks, W.F., Hibler, W.D., 2010. Appendix E: Thin sections. On Sea Ice. Univ.. Alaska Press, 566—570.

Weeks, W F, Gow, A, Kosloff, P., Digby-Argus, S., 1990. The internal structure, composition and properties of brackish ice from the Bay of Bothnia. In: Ackley, S.F., Weeks, Wilford F. (Eds.), Sea Ice Properties and Processes: Proc. W.F. Weeks Sea Ice Symp., CRREL Monogr., 5—15.

Zibordi, G., Darecki, M., 2006. Immersion factors for the RAMSES series of hyper-spectral underwater radiometers. J. Opt. A Pure Appl. Opt. 8, 252—258, https://doi.org/10.1088/1464-4258/8/3/005.